Urban Particulate Matter Triggers Meibomian Gland Dysfunction

Mengqian Tu, Ren Liu, Jianwen Xue, Bing Xiao, Jing Li, and Lingyi Liang

State Key Laboratory of Ophthalmology, Zhongshan Ophthalmic Center, Sun Yat-Sen University, Guangdong Provincial Key Laboratory of Ophthalmology and Visual Science, Guangzhou, China

Correspondence: Lingyi Liang, Zhongshan Ophthalmic Center, State Key Laboratory of Ophthalmology, 7 Jinsui Road, Guangzhou 510060, China;
lianglingyi@gzzoc.com.

MT and RL contributed equally as co-first authors.

PURPOSE. The meibomian gland (MG), as the largest modified sebaceous gland, is potentially damaged by urban particulate matter (UPM) based on epidemiological evidence, but the specific experimental mechanisms remain unknown. This study investigated the effects of UPM on MG dysfunction (MGD) in rodent models.

METHODS. Female C57BL/6J mice received eye drops containing UPM suspension or PBS for 14 days. The proliferative capacity and progenitor of MG were evaluated by immunofluorescence. Cell apoptosis was confirmed by TUNEL assay, along with the analysis of caspase family expression. Lipid accumulation was visualized by Oil Red O staining and LipidTox staining. Ductal hyperkeratinization, neutrophil infiltration, and pyroptosis activation were detected through immunostaining. The relative gene expression and signaling pathway activation were determined by Western blot analysis.

RESULTS. Administration of UPM caused MGD-like clinical signs, manifested as distinct corneal epithelial erosion, increased MG orifice occlusion, and glandular dropout. UPM exposure significantly induced progenitor loss, cellular apoptosis, and lipogenic disorder in MG, by reducing P63/Lrig1 expression and increasing cleaved caspase-8, -9, and -3 and meibum lipogenic protein (HMGCR/SREBP-1) expression. UPM-treated mice exhibited ductal hyperkeratinization and neutrophil recruitment. Simultaneously, pyroptosis was motivated, as indicated by the heightened expression of NLRP3 and the cleavage of caspase-1 and -4 and gasdermin D, as well as the increase in IL-1β and IL-18 downstream. The underlying pathological mechanisms of UPM involve the phosphorylation of mitogen-activated protein kinase and nuclear factor-κB.

CONCLUSIONS. These results provided direct evidence for the toxicity of UPM in MG. UPM-induced activation of pyroptosis and mitogen-activated protein kinase/nuclear factor-κB signaling pathway might account for the inflammatory MGD.

Keywords: urban particulate matter, meibomian gland, meibomian gland dysfunction, inflammation, pyroptosis

Air pollution is an increasingly serious global health issue, that poses a major threat to human well-being.[1,2] Particulate matter was classified as a Group 1 human carcinogen by the International Agency for Research on Cancer in 2013.[3] In the matter of the potential hazards of air pollutants on human health, urban particulate matter (UPM) is a major concern.[4] UPM carries various toxic substances, including heavy metals, endotoxin, nitrogen oxides, and polycyclic aromatic hydrocarbons,[5] which have been found to be genotoxic, mutagenic, and carcinogenic and can induce severe inflammatory responses in multiple human organs.[6] Extensive research has shown a strong correlation between air pollutants and higher rates of respiratory and cardiovascular diseases, leading to increased mortality and morbidity.[7,8] Additionally, the economic burden associated with these health conditions is substantial.[9]

The eyes are one of the few organs directly and continuously exposed to the external environment, making the microenvironment of the ocular surface vulnerable to damage from airborne particulate matter.[10] Epidemiologi-cal evidence indicates that individuals living in areas with high levels of air pollution often complain of ocular disorders such as ocular itching, foreign body sensation, burning, and redness.[11,12] Clinical observations in ophthalmology have further established a strong association between UPM and an increased incidence of various ocular surface inflammatory diseases, including allergic conjunctivitis,[13,14] keratitis,[15] and dry eye disease.[16] Noticeably, a recent prospective multicenter study reported a positive correlation between UPM exposure and decreasing meibum quality and meibomian gland (MG) dropout frequency, indicating that UPM may also exert a role in MG dysfunction (MGD) pathophysiology.[17] However, the toxic effect of UPM on the MG remains largely unclear, as previous experimental studies primarily focused on its effects on inflammatory responses, proliferation, and apoptosis in corneal[18,19] and conjunctival epithelial cells.[20,21]

The MG (the largest modified sebaceous gland) consists of ducts and tufted lipogenic acini arranged parallelly and vertically in the upper and lower eyelids.[22] The MG is

a holocrine lipid-excreting gland with a central duct that opens at the eyelid margin and is composed of progenitor, differentiated (meibocytes), and ductal epithelia cells.[23,24] Matured meibocytes undergo lipid droplet accumulation and cell disintegration before releasing a lipid-enriched mixture (meibum) into the MG central duct, which is further transported to the ocular surface, formatting the tear film lipid layer.[22,25] Therefore, any risk factors that arouse MG terminal duct obstruction and/or qualitative or quantitative changes of meibum will induce MGD.[26]

MGD is the leading cause of evaporative dry eye, resulting in tear film instability, increased tear evaporation, elevated tear osmolarity, and associated ocular inflammation.[27] MGD has become a quite prevalent disorder with an estimated pooled worldwide prevalence of approximately 35.8%.[28] In certain regions, such as China,[29] Spain,[30] and Japan,[31] the incidence of MGD exceeds 50%. MGD symptoms, including eye foreign body sensation, eye irritation, visual disturbances, and other related symptoms, significantly impact human quality of life.[32,33]

Although the exact pathogenic mechanism of MGD remains unclear, recent studies have suggested that inflammation plays a crucial role in its development by influencing the structure and function of MG.[34] In comparison with healthy controls, patients with MGD presented inflammatory cell infiltration around the acini,[35,36] which has been confirmed in MGD mice to result in glandular dropout, abnormal meibum secretion, and ductal obstruction.[37,38] Of particular interest, UPM is a particularly important inflammatory inducer for the inflammatory potential of PM output in various diseases,[39] and UPM exposure has been associated with increased levels of the proinflammatory factors IL-1β, IL-8, and TNF-α were also detected in the tear samples from the individuals exposed to UPM.[40] Studies investigating the mechanism of UPM-induced corneal damage, reported the activation of the NOD-like receptor family containing the three pyrin domains (NLRP3) inflammasome and subsequent NLRP3-mediated pyroptosis in vitro and in vivo, which induced the release of proinflammatory cytokines and triggered an inflammatory cascade reaction.[41] Therefore, we conducted this research to investigate MGD-like inflammatory damage associated with UPM exposure along with the underlying mechanism.

Our results demonstrated that long-term exposure to UPM remarkably impaired ocular health, and caused structural and functional damage to the MG. UPM exposure strongly activated the pyroptosis pathway along with inflammatory reactions were strongly stimulated. This study is the first to elucidate the involvement of UPM in MG degeneration, and identify the major roles of pyroptosis and the related inflammatory response in UPM-induced MGD.

METHODS

Acquisition of UPM (SRM 1648A)

The standard reference material of UPM (SRM 1648a) was collected in St. Louis, Missouri, and obtained from the National Institute of Standards and Technology. SRM 1648a was used in this study to guarantee the reproducibility of experiments, whose properties and characteristics, as well as the preparation methods have been described previously.[42] UPM powder naturally existed before the processing and was stored in its original amber glass bottle at room temperature according to the instruction, away from sources of radiation, including ultraviolet lamps or sunlight. UPM went through resuspension of the resulting concentration of 12 mg/mL in PBS, and vortex with ultrasound before use.

Animals

The GemPharmatech Co., Ltd. (Nanjing, China) provided all the 20 female C57BL/6J wild-type mice (6–8 weeks of age, 17–22 g) used in the study. All the animals had ad libitum access to standard rodent feed and water and were kept in a standard pathogen-free condition on alternating 12-hour light/dark cycles from 8:00 AM to 8:00 PM, with 60% ± 5% humidity and a 23°C ± 1°C room temperature. Animal care and experimental procedures conformed to the statement of the ARVO on the use of animals in ophthalmic and vision research. All animal studies were approved by the Institutional Animal Care and Use Committee of Zhongshan Ophthalmic Center, Sun Yat-Sen University (Approval number: Z2022-024). Before the experiment, animals were isolated and acclimated for 1 week and were confirmed to be free of any ocular diseases.

Study Groups and UPM Exposure

Animals were divided randomly into two groups (10 mice per group), whose right eyes were topically applied 12 mg/mL UPM in PBS (3 × 2 µL) or PBS (3 × 2 µL) four times per day at 9:00 AM, 12:00 PM, 3:00 PM, and 6:00 PM for 14 consecutive days. The frequency and duration of PM treatment were previously determined in a pilot trial, and the dose was determined based on the average concentration over a 24-hour period that was considered to be a risk to the entire population.[43,44] After each eye drop, the eyelids of the mice were manually closed several times to ensure that the UPM was evenly covered on the ocular surface of the mice. All mice were euthanized on day 15 after the treatment.

Animal Examination

The eyelid margins and corneas of animals were monitored and photographed under a slit-lamp microscope (Topcon SL-D701, Tokyo, Japan) at day 0 and day 15 by a single masked ophthalmologist after they were weighted. All mice were anesthetized with an intraperitoneal injection of 1% sodium pentobarbital (50 mg/kg) before a routine examination of the ocular surface. To perform the corneal fluorescein staining, all mice were applied 2 µL of 0.5% sodium fluorescein, by instillation into the conjunctival sac. After manual eyelid closure three times, the mice's corneas were observed and photographed under cobalt blue lights in the slit lamp microscope. As previously reported, the cornea was divided into four quadrants, each scored separately, and the four scores were summed to obtain the final grade (total, 16 points). The fluorescein score of each quadrant was analyzed as follows: 0, absent; 1, slightly punctate staining (<30 spots); 2, punctate staining (>30 spots, but not diffuse); 3, severe diffuse staining but no positive plaque; and 4, positive fluorescein plaque.[45]

After being euthanized, each mouse had the upper and lower eyelids of the treated eye were excised integrally, and the MGs were isolated by removing the eyelid skin, subcutaneous tissue, muscle, and hair follicles. We randomly selected four mice from each group, whose harvested MGs were all used for Western blot analysis. Meanwhile, the

isolated MGs of the remaining 12 mice were all used for morphological examination. The MGs were photographed with a stereoscopic zoom microscope (Zeiss SteRo Discovery v8, Jena, Germany) and the areas of MGs were measured by ImageJ (National Institutes of Health, Bethesda, MD, USA). After taking the photograph, MGs harvested from the remaining 6 mice in each group were randomly selected for paraffin sections, sagittal, and coronal frozen sections.

Histology

MG tissues were fixed with 4% paraformaldehyde and subsequently embedded in optimal cutting temperature after a series of sucrose gradients (10%, 20%, of 30%), or in paraffin after dehydrated by an alcohol gradient (75%, 85%, 95%, 100%, or 100%) and cleared with xylene. Frozen sections, cut into sagittal and coronal sections with a thickness of 8 µm and stored at −80°C, were prepared for Oil Red O staining, LipidTox staining, and immunofluorescence staining. Hematoxylin and eosin staining and immunohistochemical staining were performed on paraffin sections, which were cut into sagittal sections (4 µm thick), and stored at room temperature.

Oil Red O Staining

Oil red O staining solution was configured before the staining. Then the sagittal frozen MG sections were washed four times in PBS (5 minutes each time), treated with 60% 2-propanol for 30 seconds, and stained in freshly prepared Oil Red O solution for 10 minutes. After decolorization with 60% 2-propanol for 3 minutes, the sections were counterstained with hematoxylin and mounted in 90% glycerol. Images were acquired using Tissue FAXS Q+ (TissueGnostics, Vienna, Austria).

LipidTox Staining

After being washed four times for 5 minutes in PBS, the sagittal frozen sections of MG were stained with neutral lipid droplet with HCS LipidTox solution (1:500, H34475; Invitrogen, Grand Island, NY, USA) for 30 minutes at room temperature. To visualize the nuclei of the cell, sections were then counterstained with 4′,6-diamidino-2-phenylindole (DAPI, 1 µg/mL; Biofroxx, Einhausen, Germany) for 15 minutes. LipidTox staining images of representative areas of the MG were obtained with the confocal laser scanning microscope (LSM 980; Zeiss, Oberkochen, Germany).

Immunohistochemical Staining

Paraffin sections were deparaffinized in xylene solution, rehydrated in a decreased alcohol series, and incubated in 10 mmol/L sodium citrate buffer at 80°C for 10 minutes, followed by cooling to room temperature for antigen retrieval of immunostaining. To block endogenous peroxidase activity, sections were treated with 3% hydrogen peroxide and blocked with PBS plus 0.1% Tween-20 (PBST) containing 10% donkey serum. The sections were then incubated overnight with primary rabbit antibodies: HMGCR (1:1000, A16875; Abclonal, Wuhan, China), cleaved caspase-3 (1:50, 9664S; Cell Signaling Technology, Boston, MA, USA), neutrophil elastase (NE) (1:100, ab68672 Abcam; Cambridge, MA, USA), and CD45 (1:100, 70257S; Cell Signaling Technology). After being washed with PBS, MG sections were incubated with horseradish peroxidase-conjugated secondary antibody (1:1000, ab6802; Abcam), counterstained with hematoxylin, and then captured by Tissue FAXS Q+.

Immunofluorescence Staining

Sagittal and coronal sections of MG tissues were permeabilized in 0.2% Triton X-100 and then blocked with PBS containing 3% BSA (Sigma-Aldrich, St Louis, MO, USA). The primary antibodies used in this step of overnight incubation included rabbit anti-Ki67 (1:150, MA5-14520; Invitrogen), rabbit anti-P63 (1:100, ab124762; Abcam), goat anti-Lrig1 (1:100, AF3688; R&D Systems, Minneapolis, MN, USA), rabbit anti-NLRP3 (1:100, NBP2-12446; R&D Systems), rabbit anti-cleaved caspase-1 (1:100, A0964; Abclonal), rabbit anti-gasdermin D (GSDMD) (1:100, A18281; Abclonal), rabbit anti-NE (1:100, A13015; Abclonal), and mouse anti-cytokeratin 6 (K6) (1:100, ab18586; Abcam) for sagittal sections, whereas rabbit anti-cytokeratin 1 (K1) (1:50, ab185628; Abcam), rabbit anti-cytokeratin 10 (K10) (1:50, ab76318; Abcam) for coronal sections. The following fluorophore-conjugated secondary antibodies were used for the subsequent incubation of the slides in the dark at room temperature for 1 hour: Alexa Fluor 488– or Alexa Fluor 555–labeled donkey anti-rabbit IgG antibody (1:500, 488-ab150073, 555-ab155062; Abcam), Alexa Fluor 647–labeled donkey anti-goat IgG antibody (1:500, ab150135; Abcam), and Alexa Fluor 488–labeled donkey anti-mouse IgG antibody (1:500, ab150105; Abcam). The slides were incubated with DAPI for 15 minutes under the same conditions as the secondary antibodies and then captured using a confocal laser scanning microscope LSM 980.

TUNEL Assay

The apoptosis of frozen eyelid sections was detected using TUNEL FITC Apoptosis Detection Kit (Vazyme, Nanjing, China) according to the manufacturer's instructions. Briefly, the frozen sections were first fixed with 4% paraformaldehyde for 30 minutes and incubated with proteinase-K for 10 minutes. After being incubated in a buffer for a 10-minute equilibration, sections were added with the TUNEL reaction mixture and kept at 37°C for 1 hour in a humidified dark room followed by the counterstain of DAPI. The digital images of TUNEL-positive cells were photographed with the confocal laser scanning microscope LSM 980.

Protein Extraction and Western Blot

For protein extraction, the upper and lower MGs of the treated eye of a mouse were combined to form a protein sample. Then the freshly isolated and finely cut MGs were immediately placed into a cold RIPA lysis buffer containing phenylmethylsulfonyl fluoride and phosphatase inhibitor cocktail (all purchased from Sigma-Aldrich). Protein concentrations in each group were measured by a BAC protein assay kit (Solarbio, Beijing, China). A total of 25 µg protein was loaded into a 4% to 20% SDS-PAGE gel for electrophoresis and transferred onto a polyvinylidene fluoride membrane through the electroblotting system (all bought from Bio-Rad, Hercules, CA, USA). The membrane was then blocked in 3% BSA for 2 hours and immunoblotted with primary antibodies overnight: rabbit anti-HMGCR (1:1000, A16875), rabbit anti-SREBP-1 (1:1000, ab3259; Abcam), goat anti-Lrig1 (1:1000, AF3688), rabbit anti-K1 (1:1000, ab185628), rabbit

anti-K10 (1:1000, ab76318), rabbit anti-cleaved caspase-8 (1:1000, 8592T; Cell Signaling Technology), rabbit anti-cleaved caspase-9 (1:1000, 20750S; Cell Signaling Technology), rabbit anti-cleaved caspase-3 (1:1000, 9664S), rabbit anti-NLRP3 (1:500, NBP2-12446), rabbit anti-caspase-1 and rabbit anti-cleaved caspase-1 (1:1000, A0964), rabbit anti-GSDMD (1:1000, A18281), rabbit anti-cleaved GSDMD (1:1000, ab209845; Abcam), rabbit anti-IL-18 (1:1000, A1115; Abclonal), rabbit anti-IL-1β (1:1000, ab234437; Abcam), rabbit anti-caspase-4 and rabbit anti-cleaved caspase-4 (1:1000, NBP3-13397; R&D Systems), rabbit anti-C5/C5a (1:1000, A8104; Abclonal), rabbit anti-matrix metalloproteinase-9 (MMP-9) (1:1000, A2095; Abclonal), rabbit anti-TNF-α (1:1000, A0277; Abclonal), rabbit anti-p65 (1:1000, 8242S; Cell Signaling Technology), rabbit anti-phospho-p65 (1:1000, 3033S; Cell Signaling Technology), rabbit anti-p38 (1:1000, 8690S; Cell Signaling Technology), rabbit anti-phospho-p38 (1:1000, 4511S; Cell Signaling Technology), rabbit anti-β-actin (1:2000, 4970S; Cell Signaling Technology), rabbit anti-GAPDH (1:2000, 5174S; Cell Signaling Technology). Immunodetection of the membrane was conducted with horseradish peroxidase-conjugated goat anti-rabbit IgG antibody (1:5000, ab6378; Abcam) or donkey anti-goat IgG antibody (1:5000, ab6885; Abcam), visualized with enhanced chemiluminescence reagents. Bands of each interested protein were observed and recorded by the Bio-Rad Gel Doc XR Gel Documentation System, and analyzed through Image Lab 5.1 software (Bio-Rad).

Image Processing and Statistical Analysis

The immunocytochemistry and immunofluorescence data were collected and quantified by Image J. Specifically, the immunofluorescence analysis of Ki67, P63, and TUNEL was performed by calculating the ratio of positive cells to DAPI-stained nuclei of MGs. The LipidTox fluorescence intensity depicted in the article is derived from the ratio of the integrated density of stained glands to the area of the high-power field of view. To guarantee the reliability of the experimental results and avoid accidental experiment outcomes, we ensured a total of four biological replicate samples in both immunohistochemistry and immunofluorescence results. Additionally, we used at least six captured images in each biological replicate sample for statistical analysis.

The statistical significance of all quantitative data from the two groups was determined by unpaired two-tailed Student *t* tests and performed with Prism software version 8 (GraphPad Software, La Jolla, CA, USA). Summary data are presented as means $\pm$ SD. A *p* value of less than 0.05 was identified as statistically significant.

RESULTS

UPM-Induced Pathological Change in Eyelid and Ocular Surface

To investigate the potential induction of MGD pathological changes by UPM exposure, we used slit lamp photography to observe typical characteristic features of MGD, including ductal obstruction, glandular dropout, and corneal epithelial defect. The slit lamp images showed that the orifices of the MG central ducts in the control group appeared as small circular areas at the eyelid margins lacking pigmentation, whereas the UPM-treated group exhibited raised white

domes protruding above the surface of the eyelid margins (Fig. 1A, *red arrows*). This accumulation of lipids at the eyelid margin is a striking indicator of obstructive MGD. The stereoscopic microscope revealed obvious glandular dropout with disordered acini and ducts in both the upper and lower glands of UPM-exposed mice compared with the dense and organized MGs in control mice (Fig. 1B, *black arrows*). Quantitative analysis of the MG area revealed a decrease in acini size after 14 days of UPM exposure (*p* < 0.001) (Figs. 1E, 1F). Slit lamp images also demonstrated a notable amount of punctate corneal staining in UPM-exposed mice (Fig. 1C), along with a marked increase in the corneal fluorescein staining score (*p* < 0.001) (Fig. 1D). These results collectively suggested that exposure to UPM might lead to ocular surface damage associated with MGD.

UPM Inhibited the Proliferation of MG Cells

The continuous disintegration of terminal differentiated meibocytes during meibum holocrine secretion necessitates the constant renewal of progenitor cells to maintain the structure and acinar function of MG.[22,46] A decrease in the proliferative capacity of progenitor cells can promote the loss of functional acinar in MGD.[27] We conducted immunofluorescence staining for Ki67 to assess the proliferative capacity of MG and found that the acini of UPM-treated mice had a lower number of Ki67-positive cells than those of control mice (*p* < 0.001). P63 and Lrig1 were both important biomarkers for basal epithelial progenitor cells in human MG which represented the actively proliferating acinar basal cells and fed new differentiating meibocytes into the developing MG.[47,48] Immunofluorescence images demonstrated a marked reduction in the number of P63-labeled cells and the level of Lrig1 in the acini of UPM-treated mice (*p* < 0.001) (Figs. 2C–2E). The UPM-treated group showed a 0.62-fold lower expression of Lrig1 protein than the control group (Figs. 2F, 2G) (both *p* < 0.01), revealing the attenuated proliferation and impaired renewal of MG functional cells. These results suggested that UPM might contribute to acinar dropout in MGD by inhibiting cell proliferation in MG.

UPM Exposure Enhanced Apoptosis in MG Cells

As a holocrine gland, the terminal differentiation of MG acinar cells is regulated by programmed cell death[49]; therefore, we examined cell apoptosis in MG by TUNEL staining. The MG cells of control mice exhibited minimal apoptosis, while the number of TUNEL-positive cells increased significantly in the MG cells of UPM-treated mice (Figs. 3A, 3B). Immunohistochemical staining also showed that UPM exposure upregulated cleaved caspase-3 expression in acinar cells (Fig. 3C). Western blot analysis confirmed that UPM exposure promoted the cleavage of caspase-8 (2.59-fold; *p* < 0.01), caspase-9 (2.34-fold; *p* < 0.001), caspase-3 (2.94-fold; *p* < 0.05) compared with that in the control group (Figs. 3D–G). These findings indicated that UPM treatment induced apoptosis in MG, suggesting an increased rate of differentiation-related cell death in meibocytes.

UPM Exposure Induced Meibum Metabolism Disorder of the MG

The abnormal terminal differentiation of meibocytes suggested that obstructive MGD was potentially mediated
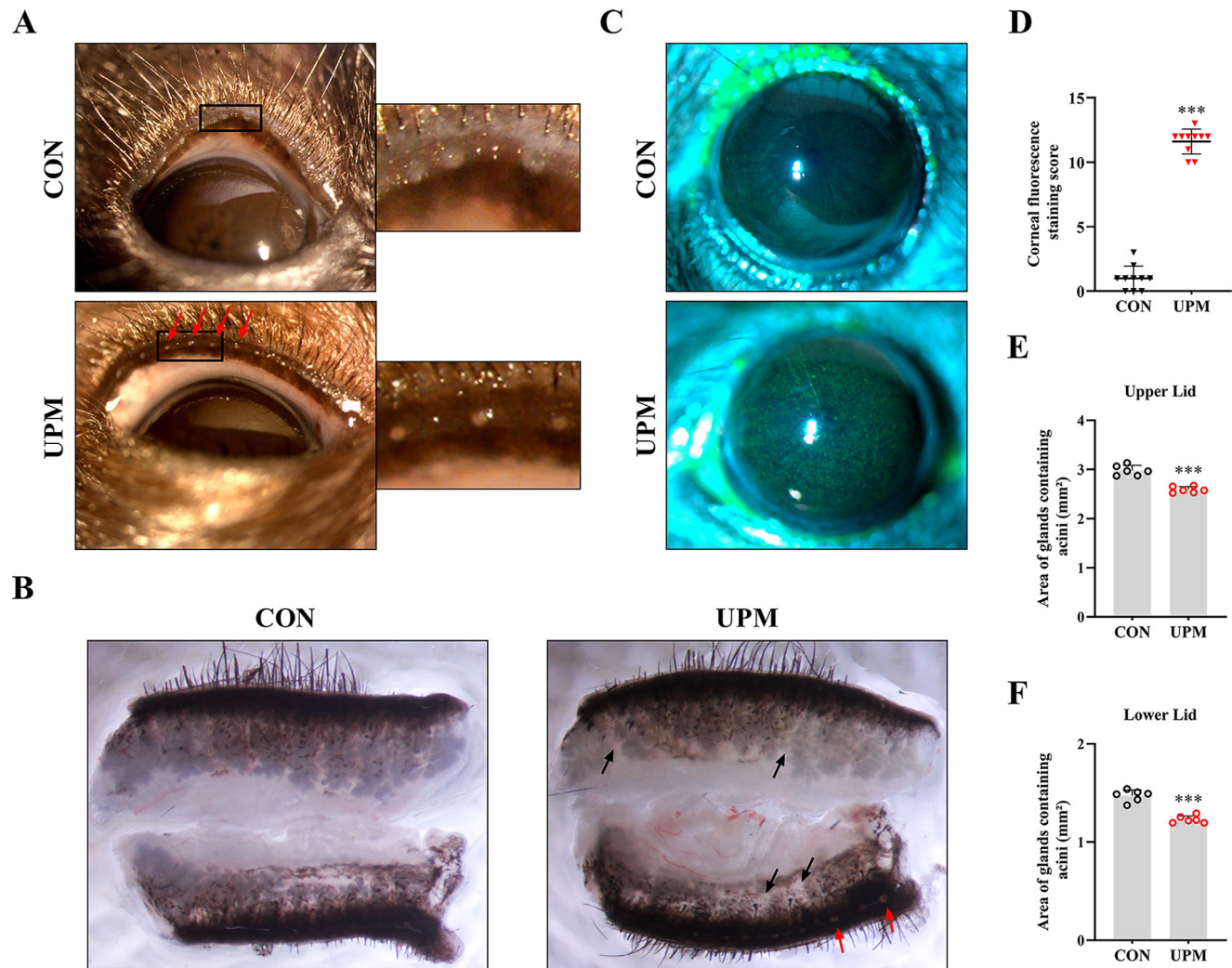
FIGURE 1. UPM-treated mice exhibited clinical evidence of MGD. UPM-treated and PBS-treated mice were compared using (**A**) slit-lamp observation (*red arrows* indicated MG duct obstruction) after the treatment, (**B**) stereoscopic microscope examination (*black arrows* indicated MG atrophy, *red arrows* indicated MG orifice blockage), and (**C**) cornea fluorescein staining (n = 10 mice per group). (**D**) The fluorescein staining score increased (n = 10 mice per group) and the area of glands containing acini in the (**E**) upper and (**F**) lower lids decreased in UPM-treated mice (n = 6 mice per group). Data are shown as mean ± SD of at least three independent experiments; ***$p < 0.001$.

by a meibum lipids disorder. Therefore, we conducted Oil Red O staining and LipidTox Green staining to observe the distribution of meibum lipids in MG. Oil Red O staining showed that the lipids were diffusely distributed in the acini and condensed in the ducts. However, the MGs of the UPM-treated mice exhibited more condensed staining of meibum-filled acinar cells (Fig. 4A). Similarly, LipidTox Green staining identified bulk lipid deposits within the central duct region of MGs in UPM-treated mice compared with control mice (Fig. 4B), which was consistent with the mean fluorescence intensity ($p < 0.01$) (Fig. 4C).

Obstructive MGD has been reported to be associated with an inordinate increase in the amount of cholesterol in the meibum.[50] Therefore, we evaluated the expression of key meibum lipogenic regulators including 3-hydroxy-3-methylglutaryl coenzyme A reductase (HMGCR) and sterol regulatory element-binding protein 1 (SREBP-1), which are responsible for the synthesis of cholesterol in meibum.[50,51] We first used immunohistochemical staining to observe the distribution and expression of HMGCR in MGs after

UPM treatment. In control mice, the expression of HMGCR was concentrated in the basal cells of acini and progressively decreased as cells matured, whereas UPM treatment markedly promoted HMGCR expression in acinar cells (Fig. 4D). Western blot analysis further confirmed that the protein levels of both HMGCR and SREBP-1 were prominently increased in UPM-exposed MGs (Figs. 4E–G; both $p < 0.001$), suggesting the enhanced lipogenesis of cholesterol.

UPM Exposure Caused Ductal Hyperkeratinization in MG

Hyperkeratinization of ductal epithelium is another major driver of excretory duct obstruction, meibum secretion inhibition, and degenerative dilatation and atrophy of MG acini in obstructive MGD.[22] We investigated whether UPM induced MG ductal keratinization based on the expressions of K1 and K10, which are biomarkers for keratinized epithelium.[52,53] Immunofluorescence staining revealed an enhanced intensity for both K1 and K10 along the ducts
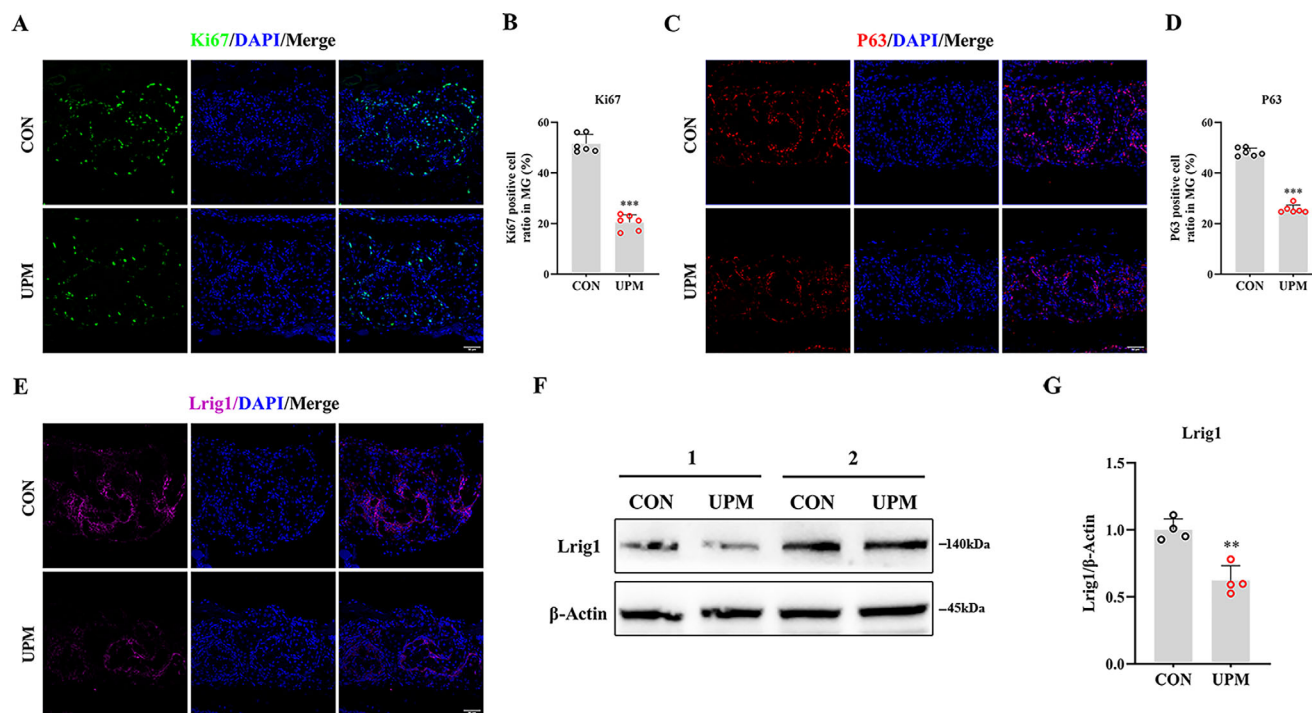
FIGURE 2. The effect of UPM exposure on acinar cell proliferation. (**A**) Immunofluorescent staining of Ki67 showed positive staining in the acinar basal cells of MG. (**B**) The bar graph showed the amount of Ki67-positive acinar basal cells/100 acinar basal cells were significantly lower in UPM-treated mice than control (n = 6 mice per group). (**C**) Immunofluorescent staining of P63 showed positive staining in the acinar basal cells of MG. (**D**) The bar graph showed the amount of P63-positive acinar basal cells/100 acinar basal cells were significantly lower in UPM-treated mice than control (n = 6 mice per group). (**E**) Representative images showed a marked decrease in Lrig1 staining in mice placed in the UPM group in comparison with those exposed to PBS. (**F, G**) Western blot analysis documented the decline in MG Lrig1 protein expression after the UPM treatment (n = 4 mice per group). Scale bars, 50 μm. Data are shown as mean ± SD. **$p < 0.01$ and ***$p < 0.001$.

in UPM-treated mice (Figs. 5A, 5B). Costaining with Lipid-Tox showed that the central duct of the MG was blocked by keratinized epithelium with a high lipid contents in UPM-exposed mice, although lipids were seen flowing normally from the central duct in control mice (Fig. 5B, *white arrows*). This result of blocked meibum discharge owing to the obstruction of the duct corresponded with the UPM-induced pathological changes in the eyelid. Western blot analysis confirmed the overexpression of K1 ($p < 0.05$) (Fig. 5D) and K10 ($p < 0.01$) (Fig. 5E) in the UPM-treated group (Fig. 5C), indicating that UPM strongly promoted hyperkeratinization in the MG.

UPM Exposure Recruited Neutrophils to the Surrounding Microenvironment of MG

The infiltration of inflammatory cells, particularly neutrophils, into the MG microenvironment participates in ductal occlusion and meibum abnormality in MGD.[54,55] Histological analysis using hematoxylin and eosin staining and CD45 immunohistochemical staining (as depicted in Figs. 6A, 6B), demonstrated increased inflammatory cell infiltration in the MGs of UPM-treated mice. Notable polymorphonuclear neutrophils (PMNs) aggregation was observed around the acini and ducts after UPM stimulation (refer to Fig. 6A, indicated by the *black arrows*). Immunohistochemical staining showed that NE a key protease mediating the inflammatory role of PMNs,[56] was positively expressed in the acini and duct of UPM-treated mice

(Fig. 6C), consistent with the immunofluorescence staining results (Fig. 6D). We verified the activation of neutrophils based on the expression of relevant proteins (Fig. 6E). C5/C5a is a chemotactic leukocyte factor and proinflammatory polypeptide that is crucial for initiating neutrophil arrest, especially in PMNs, and promotes the release of proinflammatory cytokines such as TNF-α.[57,58] We observed elevated levels of C5/C5a ($p < 0.001$) (Fig. 6F) and TNF-α ($p < 0.05$) (Fig. 6H) in the MGs of the UPM-treated mice, demonstrating an increased presence of neutrophils. We also detected the upregulation of MMP-9 expression ($p < 0.05$) (Fig. 6G), which is involved in leukocyte transendothelial migration,[58] further confirming the recruitment of activated neutrophils in UPM-stimulated MG.

NLRP3-Mediated Pyroptosis Was Triggered by UPM Exposure

Pyroptosis, a newly discovered inflammatory cell death, is an important pathway involved in the ocular toxic effects of UPM, including corneal damage[41] and glaucoma,[59] and promotes the release of numerous proinflammatory factor IL-1β. Interestingly, the IL-1β–mediated proinflammatory response has been proven to be strongly linked to abnormal lipid production and ductal pathology in MG.[60,61] To explored the underlying mechanism of UPM-induced MGD, we detected the levels of proteins involved in the pyroptosis pathway by immunofluorescence staining and Western blot. Because K6 expression is limited to ductal cells, we
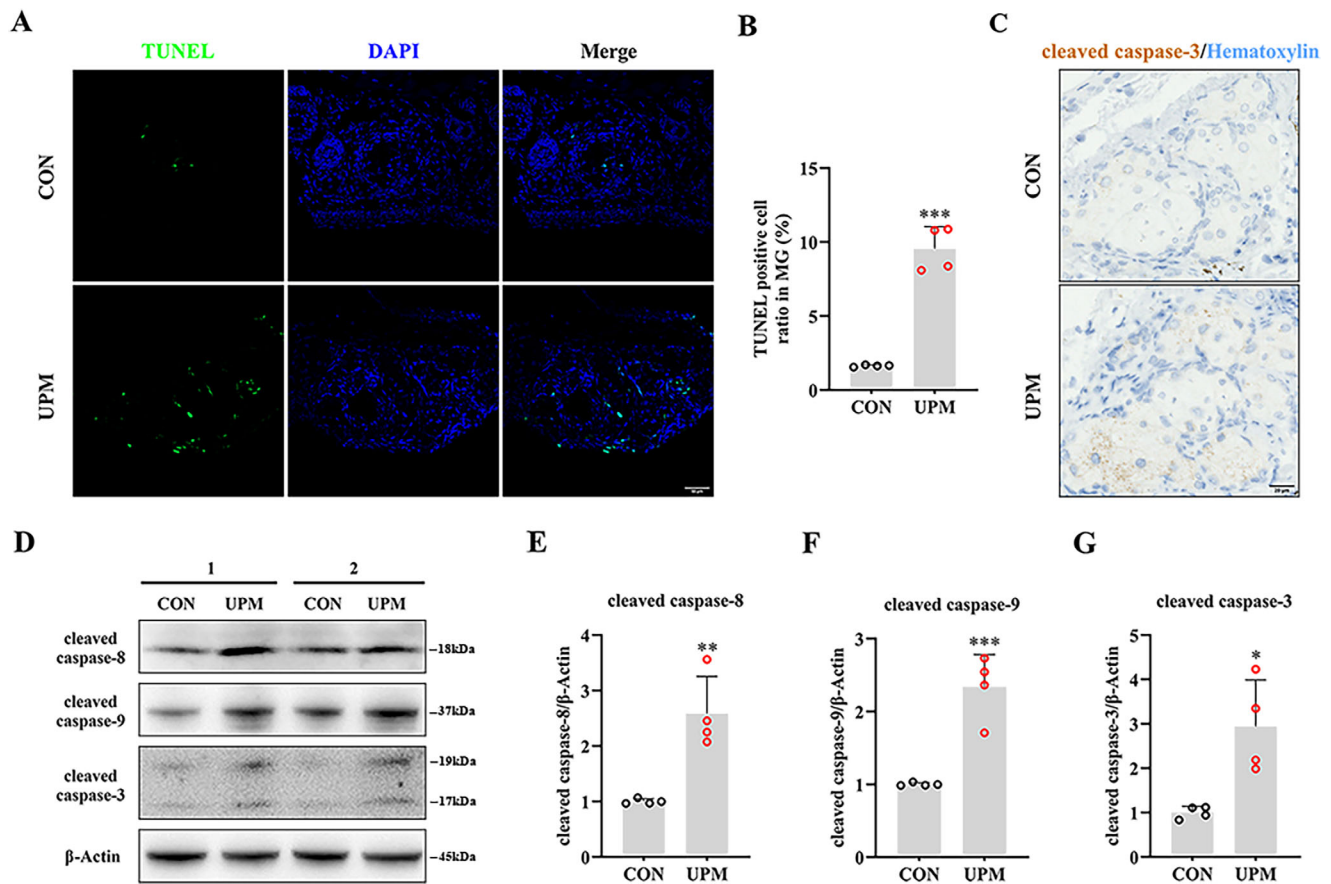
FIGURE 3. UPM-induced apoptosis through a caspase-dependent pathway. (**A**) Increased TUNEL assay staining and (**B**) cell counts revealed an increase of apoptosis cells in MGs of UPM-treated mice compared with those of the control. (**C**) Immunohistochemical staining of cell apoptosis marker cleaved caspase-3 revealed increased expression level in acini in UPM-treated mice. (**D–G**) The expression of apoptosis-related genes showed an obvious elevation of (**E**) cleaved caspase-8, (**F**) cleaved caspase-9, and (**G**) cleaved caspase-3 in UPM-treated mice (all n = 4 mice per group). Scale bars, 50 µm (**A**) and 20 µm (**C**). Data are shown as mean ± SD. *$p < 0.05$, **$p < 0.01$ and ***$p < 0.001$.

conducted counterstaining with antibodies against K6 and pyroptosis-related proteins to differentiate between ductal and acinar cells and identify the specific cell type undergoing pyroptosis.[47,62] As shown in representative images of immunofluorescence staining, NLRP3 was highly expressed and abundantly distributed in the cytoplasm of K6$^-$ acinar cells and K6$^+$ ductal cells in the UPM group compared with those in the control group at day 15 after treatment (Fig. 7A). Furthermore, the cleaved caspase-1 (Fig. 7B) and GSDMD (Fig. 7C) immunofluorescence staining were both significantly increased in two populations after the UPM exposure. The expression level of pyroptosis-related proteins was detected by Western blot. The results showed that NLRP3, caspase-1, caspase-4, and GSDMD were remarkably upregulated 1.55-fold (Figs. 7D, 7E), 1.39-fold (Fig. 7F), 1.34-fold (Fig. 7J), and 1.94-fold (Fig. 7H) after mice were treated with UPM, respectively (all $p < 0.001$). We observed the significant stimulation of caspase-1 (2.14-fold; $p < 0.001$) (Fig. 7G), caspase-4 (1.47-fold; $p < 0.01$) (Fig. 7K), and GSDMD cleavage (1.59-fold; $p < 0.01$) (Fig. 7I). Western blot analysis also revealed that exposure to UPM upregulated IL-1β (1.85-fold; $p < 0.01$) and IL-18 expression (1.80-fold; $p < 0.05$) (Figs. 7L–N). Taken together, these results suggested that UPM exerted toxic effects in MG via NLRP3 inflammasome-mediated pyroptosis, accompanied by upregulation of proinflammatory factors.

UPM Exposure Activated Nuclear Factor-κB (NF-κB) and Mitogen-Activated Protein Kinase (MAPK) Signaling Pathways

We determined whether the NF-κB and MAPK pathways, the principal upstream targets of NLRP3/GSDMD signaling,[63,64] are involved in the pathology of UPM-induced MGD through the Western blot analysis of NF-κB and MAPK components expressions. The UPM-treated group showed higher levels of NF-κB and MAPK pathway constituents than the control group (Fig. 8A). The ratios of phosphorylated to total p38 MAPK and p65 NF-κB expression were significantly increased in MGs of UPM-treated mice (Figs. 8B, 8C; both $p < 0.01$). These results suggested that the activation of NF-κB and MAPK signaling pathways might contribute to MG pyroptosis induced by UPM.

DISCUSSION

Although UPM is closely related to the clinical symptoms and signs of MGD,[17] the underlying pathological mechanisms remain unclear. This study provided the first experimental evidence of UPM-induced MGD-like changes, including punctate corneal defect, glandular dropout, meibum lipids disorder, and ductal obstruction of MG. Motivated NF-κB and
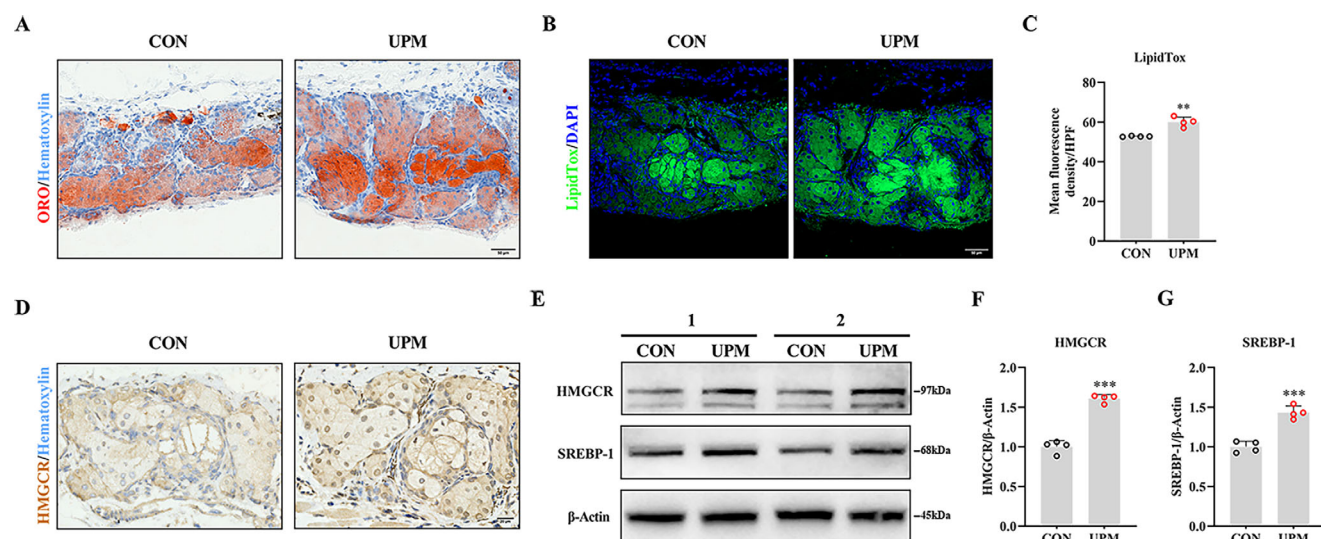
Investigative Ophthalmology & Visual Science

FIGURE 4. Meibum metabolism disorder occurred in UPM-treated mice. (**A**) The Oil Red O staining showed the distribution of lipids was characterized by diffuse distribution in acini and deposition in the central duct, and indicated the condensed staining in UPM-treated mice. The LipidTox Green staining also showed (**B**) more lipid deposits and (**C**) higher fluorescence intensity in UPM mice (n = 4 mice per group). (**D**) HMGCR expressed in MG tissue on immunohistochemistry and increased in UPM-treated mice. (**E–G**) Western blot analysis showed the expressions of (**F**) HMGCR and (**G**) SREBP-1 were both significantly increased (all n = 4 mice per group). Scale bars, 50 μm (**A, B**) and 20 μm (**D**). Data are shown as mean ± SD. $**p < 0.01$ and $***p < 0.001$.
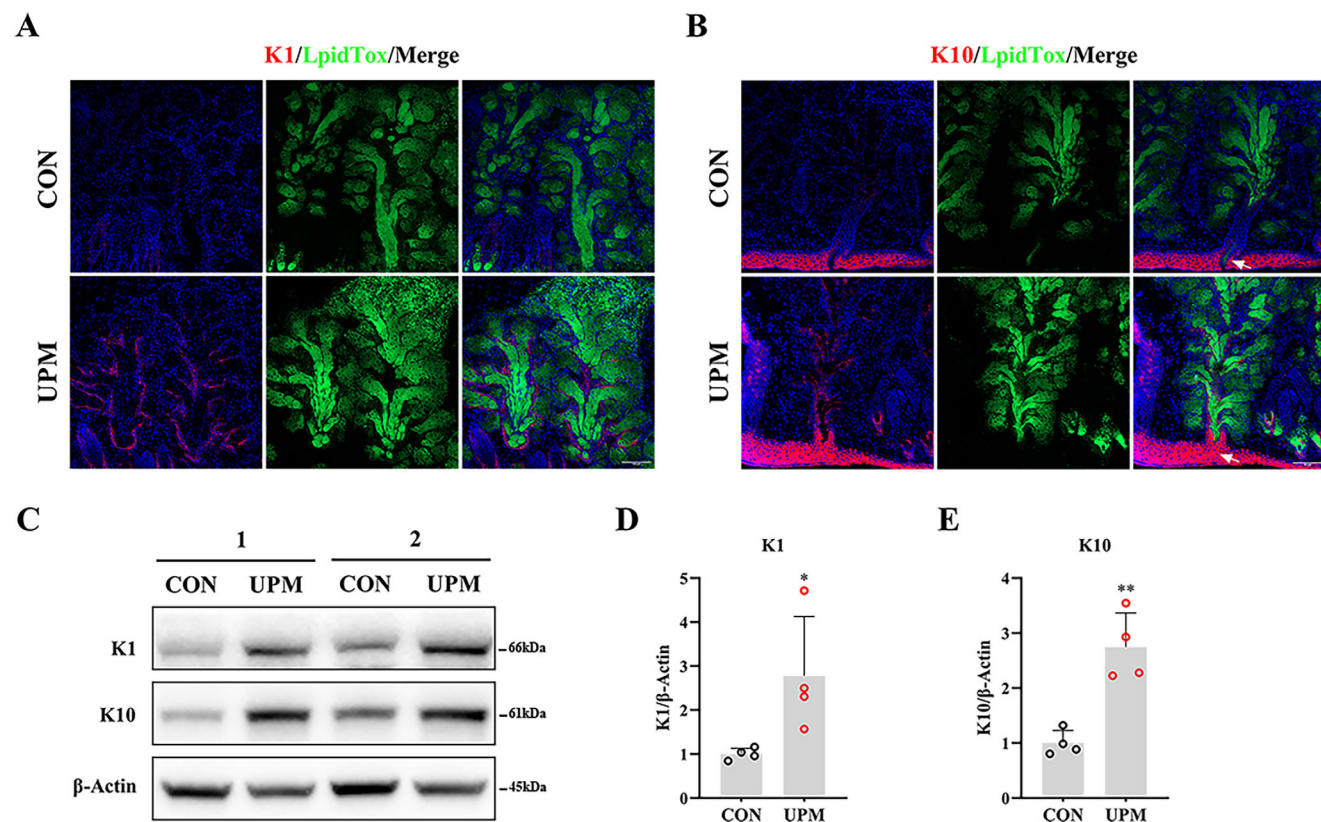

FIGURE 5. UPM-treated mice exhibited hyperkeratinization and ductal blockage. (**A, B**) Immunofluorescent staining of K1 and K10 (*red*), with lipid labeled by LipidTox (*green*), and nuclei labeled by DAPI (*blue*), showed the marked keratinization of the ductal epithelium in the UPM group, compared with the control group (*white arrows* indicated MG orifice blockage). (**C**) Representative Western blot results of keratins for mice treated with vehicle or UPM were consistent with those of staining. Relative expressions of (**D**) K1 and (**E**) K10 were both upregulated in the UPM group (both n = 4 mice per group). Scale bars, 100 μm. Data are shown as mean ± SD. $*p < 0.05$ and $**p < 0.01$.
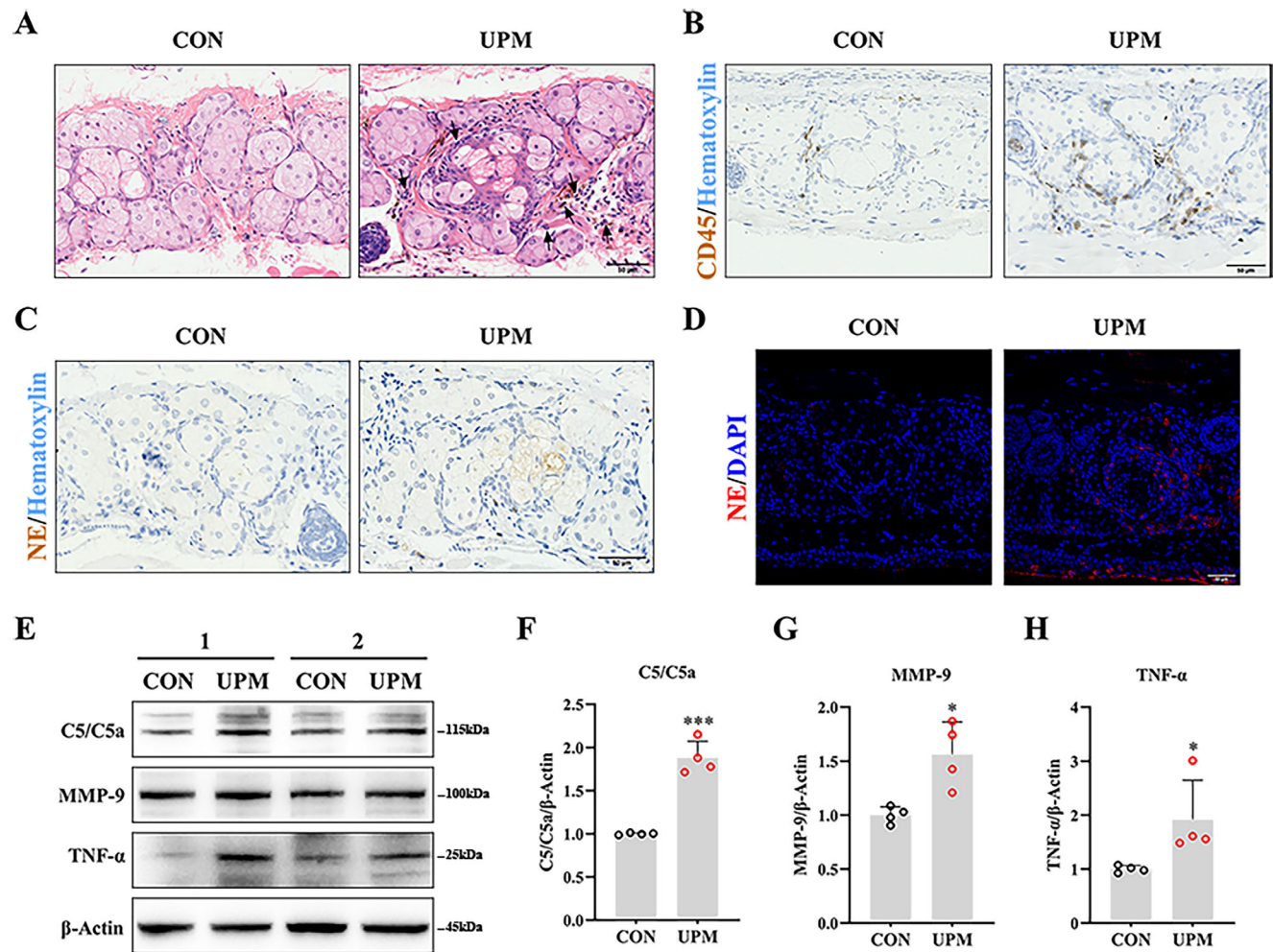
FIGURE 6. Recruitment and activation of PMNs in UPM-treated mice. (**A**) Hematoxylin and eosin staining and (**B**) immunohistochemistry showed a lot of PMNs (*black arrows*) and CD45-positive cells surrounding the MG acini. (**C**) Immunohistochemistry and (**D**) immunofluorescence of NE disclosed significant upregulation in MGs from the UPM group compared with the control group. (**E–H**) Western blot analysis of (**F**) C5/C5a, (**G**) MMP-9 and (**H**) TNF-α suggested the expression levels of these proteins were all increased (all n = 4 mice per group). Scale bars:, 50 μm. Data are shown as mean ± SD. *$p < 0.05$ and ***$p < 0.001$.

MAPK signaling pathways may play an important role in the UPM-related inflammatory response and pyroptosis in MG.

Previous epidemiological and experimental studies have implicated UPM in various ocular inflammatory diseases, especially dry eye disease, which results in decreased tear film stability and ocular discomfort.[16,65] Given that MGD is a dominant risk factor for dry eye disease and is closely linked to ocular surface discomfort and tear film instability, it is crucial to investigate the impact of UPM on MG damage.[66,67] Hao et al.[17] recently reported a positive correlation between UPM exposure and the severity of ocular surface lesions and MGD signs. Although previous studies showed that UPM induced a dose-dependent infiltration of immune cells around MG acini in an acute allergic conjunctivitis murine model (especially at concentrations of 12.8 mg/mL), the associated structural and functional alterations in the MG remained unknown.[44,68] These findings implied that exposure to high concentrations of UPM may contribute to the pathophysiology of MGD and experimental evidence was needed to elucidate the pathological process and potential therapeutic targets. In this study, the topical application of UPM suspension (12 mg/mL) caused MG orifice obstruction

and acinar atrophy in mice, consistent with clinical observations in the patients with obstructive MGD.[22,23] In addition, the corneal epithelium of the mice showed diffuse punctate erosion after UPM treatment, consistent with previous clinical findings.[69] Because continuous treatment with 12 mg/mL UPM for 14 days did not cause severe damage to the ocular surface, this model shows great potential for the direct experimental induction of MGD by UPM.

We investigated glandular dropout in UPM-related MGD, which is regarded as one of the vital pathological characteristics of MGD.[22] Glandular dropout is mainly caused by pathological accelerated differentiation of meibocytes or impaired proliferation of MG, representing a disturbance in the dynamic balance between continuous meibocytes disintegration and persistent progenitor cell supplementation.[27] UPM has been reported to not only induce the death of ovarian granulosa cells and affect ovarian reserve, but also accelerate ovarian aging by inducing cell apoptosis.[70,71] Similarly, we found that UPM exposure decreased the expression of the proliferative marker Ki67 and progenitor markers P63 and Lrig1 in MG basal epithelial cells. Furthermore, UPM also induced apoptosis in functional MG acini by activat-
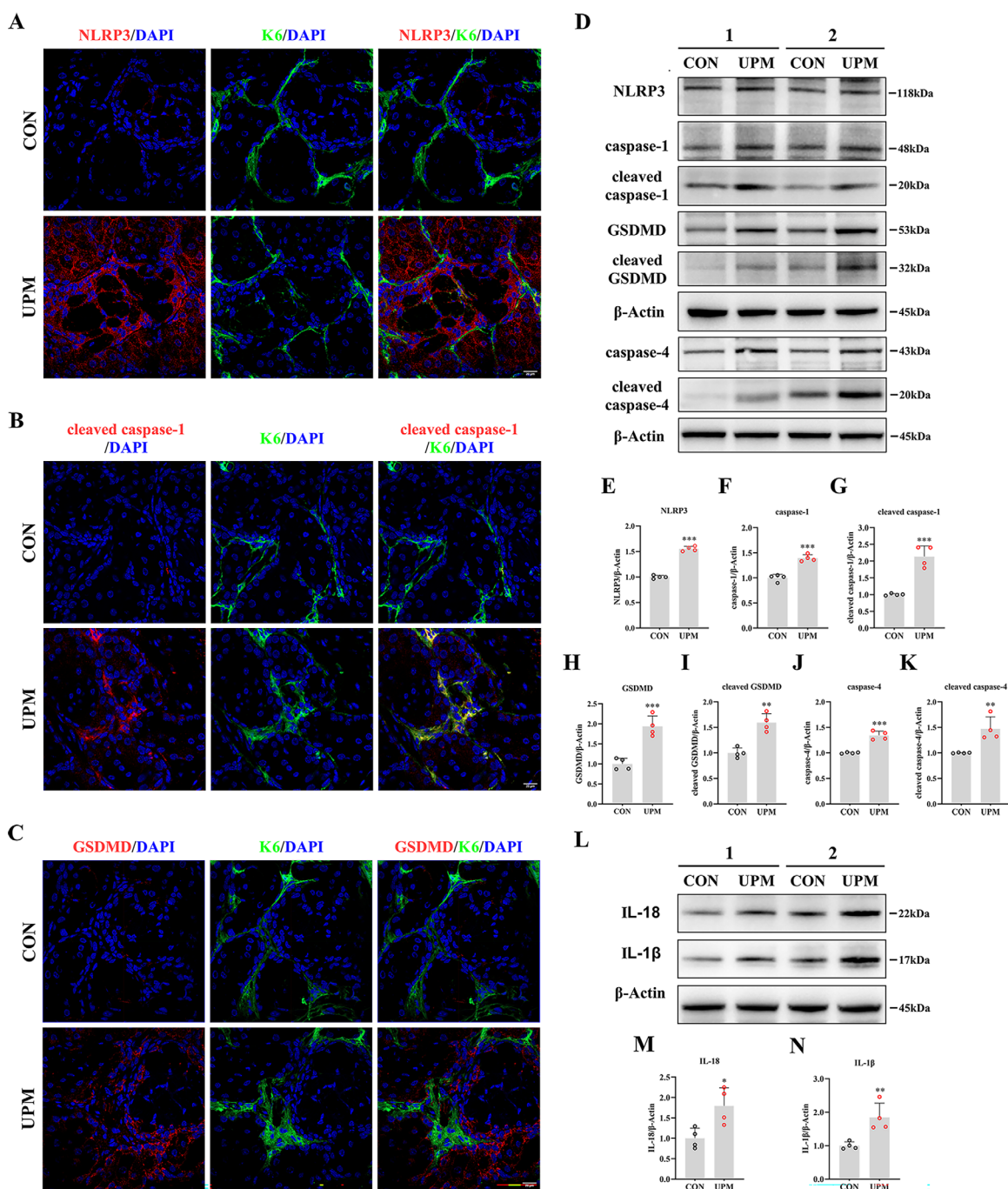
FIGURE 7. Evident pyroptosis in MG of UPM-treated mice. (**A–C**) Representative immunofluorescence images of K6 co-stained with NLRP3, cleaved caspase-1 and GSDMD. (**A**) NLRP3 was highly expressed and abundantly distributed in the cytoplasm of K6⁻ acinar cells and K6⁺ ductal cells in the UPM group. Compared with control, immunofluorescence images of (**B**) cleaved caspase-1 and (**C**) GSDMD showed increased positive cells in MG after UPM exposure. (**D**) Expressions of proteins involved in the pyroptosis pathway after treatment with vehicle or UPM. (**E–K**) Western blot quantitative analysis showed upregulation of (**E**) NLRP3 expression in MG of UPM-treated mice, and the increase of expression and cleavage of caspase-1 (**F** and **G**), GSDMD (**H** and **I**), and caspase-4 (**J** and **K**) (all n = 4 mice per group). (**L**) Representative Western blot results of IL-18 and IL-1β, and the relative expressions of (**M**) IL-18 and (**N**) IL-1β (both n = 4 mice per group). Scale bars, 20 µm. Data are shown as mean ± SD. *$p < 0.05$, **$p < 0.01$ and ***$p < 0.001$.

ing the caspase-dependent apoptotic pathway, as evidenced by the increased levels of the proapoptotic proteins cleaved caspase-8, -9, and -3. Considering the close relationship between the terminal differentiation of holocrine gland cells and apoptosis,[49] the significant activation of MG cell apoptosis induced by UPM indicated abnormally accelerated

meibocyte differentiation, which, along with the inhibition of cell proliferation in MG might contribute to glandular dropout.

UPM exposure disturbs lipid metabolism in the liver,[72,73] lung,[74] and even the cardiovascular system,[75] resulting in SREBP-1 activation, abnormal serum cholesterol levels,
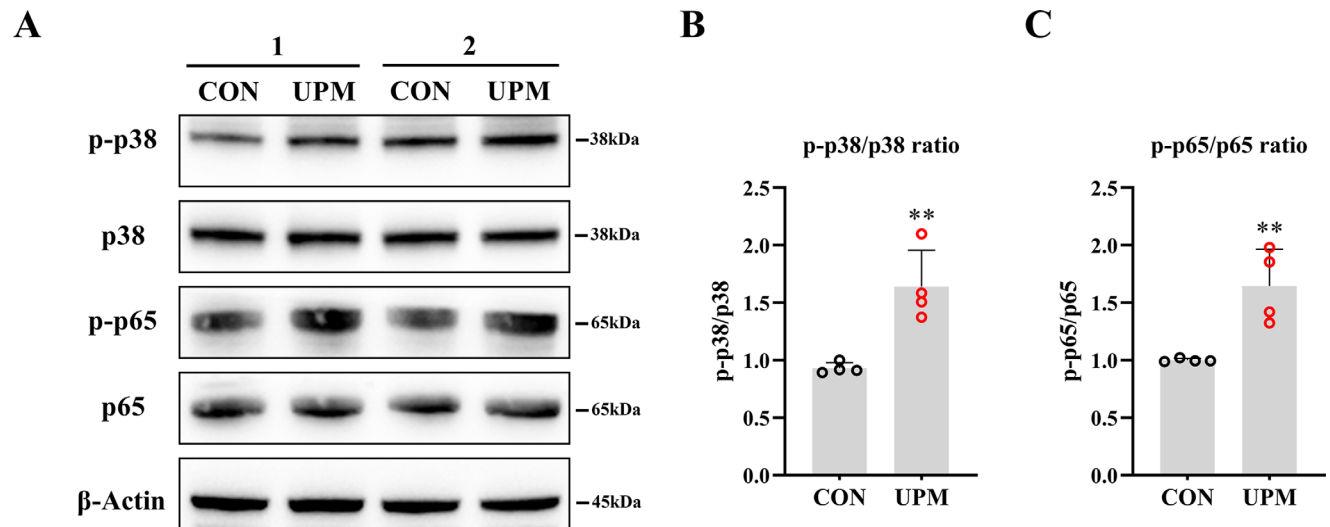
FIGURE 8. UPM activated NF-κB and MAPK signaling pathways. (**A**) Western blot analysis of p-p38 MAPK, p38 MAPK, p-p65 NF-κB and p65 NF-κB. Elevated levels of phosphorylation of (**B**) p38 MAPK and (**C**) p65 NF-κB were indicative of activated MAPK and NF-κB signaling pathways in MGs of UPM-treated mice (both n = 4 mice per group). Data are shown as mean ± SD. ** $p < 0.01$.

and lipid accumulation.[76,77] The quality and synthesis of meibum, an important actor secreted by the MG, were significantly impaired in UPM-exposed populations.[17,78] Similarly, we showed that 14 days of UPM application stimulated obvious lipid deposition within the acini and duct of MG, indicating the disorder of meibum lipid metabolism. Previous clinical studies demonstrated that the meibum of MGD patients showed a significant increase in cholesterol than healthy individuals,[50] which may be associated with the pathophysiology of MGD. We also found that the protein expressions of HMGCR and SREBP-1 involved in cholesterol synthesis were also apparently upregulated by UPM exposure. Given that the melting point of cholesterol is as high as 148°C, whereas that of meibomian secretions are only 30°C to 34°C,[79] the abnormal enrichment of cholesterol in meibum has been demonstrated to be bound up with increased viscosity, decreased fluidity, and consequent stagnation of meibum at physiological temperatures.[80] Therefore, abnormal meibum metabolism induced by UPM exposure may be an important pathogenetic factor in MGD.

Hyperkeratinization[81] of the excretory duct seems to be the initial pathological step in obstructive MGD with PMN infiltration playing a particularly important pathogenic role.[54,55] Previous studies reported that the lung overloaded with UPM led to keratinization, and lung protein cysts, as well as promoted neutrophil infiltration by triggering the inflammation response.[74,82] In our study, immunofluorescence staining of K1 and K10 revealed ductal hyperkeratinization and blockage of orifice in the MGs of mice exposed to UPM. Hematoxylin and eosin staining, CD45 immunohistochemistry, and NE immunostaining collectively indicated the presence of a large number of active PMNs in the surrounding microenvironment of MG. Surprisingly, we found that the levels of C5/C5a, MMP-9, and TNF-α proteins involved in PMNs activation, recruitment, and migration were all upregulated, supporting the contribution of PMNs infiltration in the pathogenesis of ductal obstruction caused by keratinization and the progression of obstructive MGD associated with UPM exposure.

Pyroptosis, a proinflammatory process of caspase-dependent and gasdermin-mediated programmed cell death,[83] has attracted much attention owing to its close association with the inflammation-related pathogenicity of UPM.[41,42] Under exposure to UPM, NLRP3 inflammasome-mediated pyroptotic cell death occurs followed by self-cleavage and activation of caspase-1 and -4, and eventual cell swelling and pyroptosis via GSDMD cleavage induced by cleaved caspase-1 and -4. Simultaneously, intracellular proinflammatory cytokines (e.g., IL-1β and IL-18) are released, activating the inflammatory cascade reaction.[83] NLRP3 inflammasome activation is conducive to the development of multiple systemic diseases associated with UPM exposure, not only cardiovascular,[84] respiratory,[85,86] and neurological systems,[87] but also ocular injury.[41,59] Our results showed that the activation of pyroptosis might be central to UPM-induced MG injury. UPM dramatically increased NLRP3 expression and the caspase-1 and -4 cleavage in MG. Moreover, the increased protein level and cleavage of GSDMD and upregulation of its downstream proinflammatory targets IL-1β and IL-18 in UPM-treated MG further implied that NLRP3 inflammasome-mediated pyroptosis was significantly triggered.

Activation of the NF-κB and p38 MAPK pathways could induce the formation and activation of the NLRP3 inflammasome complex, which is responsible for initiating pyroptosis through increased transcription of GSDMD and promoting inflammatory responses by upregulating levels of IL-1β and IL-18.[88] Multiple investigations have confirmed that the proinflammatory effect of UPM is often accompanied by the activation of the NF-κB and p38 MAPK pathways.[89,90] In addition, the NF-κB and MAPK pathways played an etiological role in inflammatory MGD induced by hyperglycemia[37] and hyperlipidemia in rodent models.[38] In this study, the phosphorylation of NF-κB and p38 MAPK was significantly increased in the MGs of UPM-treated mice, concurrent with pyroptosis activation and the related ductal obstruction and glandular dropout. Therefore, the activation of the NF-κB and p38 MAPK pathways might get involved in arousing the

UPM-induced MGD pathological changes associated with pyroptosis and its downstream inflammatory response.

There are also some limitations in this study. The use of UPM eye drops may not fully replicate the damage caused by air pollution, although this method is commonly used in similar studies.[19,20,59] Recent research has indicated that pyroptosis can be mitigated by inhibiting the activation of the NF-κB and p38 MAPK pathways.[88,91] Hence, further investigation is needed to determine whether the phosphorylation of NF-κB and p38 MAPK plays a pivotal role in the entire pathological process of UPM-related MGD.

This study is the first to experimentally demonstrate the toxic effects of UPM on MG *in vivo*. The activation of the p38 MAPK and NF-κB signaling pathways may contribute to the pathogenesis of UPM-induced MGD by promoting the assembly and activation of NLRP3 inflammasomes, triggering intense pyroptosis, as well as the release of numerous proinflammatory factors and subsequent inflammatory reactions. The resulting pyroptosis and inflammatory cascade reaction were associated with the pathological features of inflammatory MGD including glandular dropout, excessive lipid accumulation, and ductal obstruction. Among them, the significant reduction of progenitor cell number and inhibition of cell proliferation, along with increased cell apoptosis may account for the glandular dropout, and abnormal production of cholesterol may explain the lipid deposition, while ductal obstruction was likely due to epithelial hyperkeratinization and neutrophil aggregation. Our study provides a new perspective on the pathological mechanisms of UPM-related eye injuries, and may inform the development of clinical treatments for environment-related eye diseases.

Acknowledgments

Disclosure: **M. Tu**, None; **R. Liu**, None; **J. Xue**, None; **B. Xiao**, None; **J. Li**, None; **L. Liang**, None

References

1. Lelieveld J, Evans JS, Fnais M, Giannadaki D, Pozzer A. The contribution of outdoor air pollution sources to premature mortality on a global scale. *Nature*. 2015;525:367.

2. Health Effects of Outdoor Air Pollution. Committee of the Environmental and Occupational Health Assembly of the American Thoracic Society. *Am J Respir Crit Care Med*. 1996;153:3–50.

3. Loomis D, Grosse Y, Lauby-Secretan B, et al. The carcinogenicity of outdoor air pollution. *Lancet Oncol*. 2013;14:1262–1263.

4. Pereira G. Cut particulate air pollution, save lives. *BMJ*. 2021;375:n2561.

5. Loxham M, Nieuwenhuijsen MJ. Health effects of particulate matter air pollution in underground railway systems - a critical review of the evidence. *Part Fibre Toxicol*. 2019;16:12.

6. de Oliveira Alves N, Martins Pereira G, Di Domenico M, et al. Inflammation response, oxidative stress and DNA damage caused by urban air pollution exposure increase in the lack of DNA repair XPC protein. *Environ Int*. 2020;145:106150.

7. Samek L. Overall human mortality and morbidity due to exposure to air pollution. *Int J Occup Med Environ Health*. 2016;29:417–426.

8. Yorifuji T, Kashima S, Doi H. Associations of acute exposure to fine and coarse particulate matter and mortality among older people in Tokyo, Japan. *Sci Total Environ*. 2016;542:354–359.

9. Kelly FJ. Urban air quality and health: two steps forward, one step back. *Eur Respir J*. 2019;53:1900280.

10. Jung SJ, Mehta JS, Tong L. Effects of environment pollution on the ocular surface. *Ocul Surf*. 2018;16:198–205.

11. Gupta SK, Gupta SC, Agarwal R, Sushma S, Agrawal SS, Saxena R. A multicentric case-control study on the impact of air pollution on eyes in a metropolitan city of India. *Indian J Occup Environ Med*. 2007;11:37–40.

12. Camara JG, Lagunzad JK. Ocular findings in volcanic fog induced conjunctivitis. *Hawaii Med J*. 2011;70:262–265.

13. Mimura T, Ichinose T, Yamagami S, et al. Airborne particulate matter (PM2.5) and the prevalence of allergic conjunctivitis in Japan. *Sci Total Environ*. 2014;487:493–499.

14. Chang CJ, Yang HH, Chang CA, Tsai HY. Relationship between air pollution and outpatient visits for nonspecific conjunctivitis. *Invest Ophthalmol Vis Sci*. 2012;53:429–433.

15. Sendra VG, Tau J, Zapata G, et al. Polluted air exposure compromises corneal immunity and exacerbates inflammation in acute herpes simplex keratitis. *Front Immunol*. 2021;12:618597.

16. Mo Z, Fu Q, Lyu D, et al. Impacts of air pollution on dry eye disease among residents in Hangzhou, China: a case-crossover study. *Environ Pollut*. 2019;246:183–189.

17. Hao R, Wan Y, Zhao L, et al. The effects of short-term and long-term air pollution exposure on meibomian gland dysfunction. *Sci Rep*. 2022;12:6710.

18. Lyu D, Chen Z, Almansoob S, et al. Transcriptomic profiling of human corneal epithelial cells exposed to airborne fine particulate matter (PM(2.5)). *Ocul Surf*. 2020;18:554–564.

19. Li J, Tan G, Ding X, et al. A mouse dry eye model induced by topical administration of the air pollutant particulate matter 10. *Biomed Pharmacother*. 2017;96:524–534.

20. Yang Q, Li K, Li D, Zhang Y, Liu X, Wu K. Effects of fine particulate matter on the ocular surface: an in vitro and in vivo study. *Biomed Pharmacother*. 2019;117:109177.

21. Mu N, Wang H, Chen D, et al. A novel rat model of dry eye induced by aerosol exposure of particulate matter. *Invest Ophthalmol Vis Sci*. 2022;63:39.

22. Knop E, Knop N, Millar T, Obata H, Sullivan DA. The international workshop on meibomian gland dysfunction: report of the subcommittee on anatomy, physiology, and pathophysiology of the meibomian gland. *Invest Ophthalmol Vis Sci*. 2011;52:1938–1978.

23. Obata H. Anatomy and histopathology of human meibomian gland. *Cornea*. 2002;21:S70–74.

24. Jester JV, Nicolaides N, Smith RE. Meibomian gland studies: histologic and ultrastructural investigations. *Invest Ophthalmol Vis Sci*. 1981;20:537–547.

25. Butovich IA. Lipidomics of human meibomian gland secretions: chemistry, biophysics, and physiological role of meibomian lipids. *Prog Lipid Res*. 2011;50:278–301.

26. Foulks GN, Nichols KK, Bron AJ, Holland EJ, McDonald MB, Nelson JD. Improving awareness, identification, and management of meibomian gland dysfunction. *Ophthalmology*. 2012;119:S1–12.

27. Chhadva P, Goldhardt R, Galor A. Meibomian gland disease the role of gland dysfunction in dry eye disease. *Ophthalmology*. 2017;124:S20–S26.

28. Hassanzadeh S, Varmaghani M, Zarei-Ghanavati S, Heravian Shandiz J, Azimi Khorasani A. Global prevalence of meibomian gland dysfunction: a systematic review and meta-analysis. *Ocul Immunol Inflamm*. 2021;29:66–75.

29. Jie Y, Xu L, Wu YY, Jonas JB. Prevalence of dry eye among adult Chinese in the Beijing Eye Study. *Eye (Lond)*. 2009;23:688–693.

30. Viso E, Rodriguez-Ares MT, Abelenda D, Oubina B, Gude F. Prevalence of asymptomatic and symptomatic meibomian gland dysfunction in the general population of Spain. *Invest Ophthalmol Vis Sci*. 2012;53:2601–2606.

31. Amano S, Inoue K. Clinic-based study on meibomian gland dysfunction in Japan. *Invest Ophthalmol Vis Sci*. 2017;58:1283–1287.

32. Asiedu K, Dzasimatu S, Kyei S. Impact of meibomian gland dysfunction on quality of life and mental health in a clinical sample in Ghana: a cross-sectional study. *BMJ Open*. 2022;12:e061758.

33. Asiedu K, Dzasimatu SK, Kyei S. Impact of dry eye on psychosomatic symptoms and quality of life in a healthy youthful clinical sample. *Eye Contact Lens*. 2018;44(Suppl 2):S404–S409.

34. Mizoguchi S, Iwanishi H, Arita R, et al. Ocular surface inflammation impairs structure and function of meibomian gland. *Exp Eye Res*. 2017;163:78–84.

35. Qazi Y, Kheirkhah A, Blackie C, et al. Clinically relevant immune-cellular metrics of inflammation in meibomian gland dysfunction. *Invest Ophthalmol Vis Sci*. 2018;59:6111–6123.

36. Nien CJ, Massei S, Lin G, et al. Effects of age and dysfunction on human meibomian glands. *Arch Ophthalmol*. 2011;129:462–469.

37. Guo Y, Zhang H, Zhao Z, et al. Hyperglycemia induces meibomian gland dysfunction. *Invest Ophthalmol Vis Sci*. 2022;63:30.

38. Bu J, Wu Y, Cai X, et al. Hyperlipidemia induces meibomian gland dysfunction. *Ocul Surf*. 2019;17:777–786.

39. Wu W, Jin Y, Carlsten C. Inflammatory health effects of indoor and outdoor particulate matter. *J Allergy Clin Immunol*. 2018;141:833–844.

40. Hao R, Zhang M, Zhao L, et al. Impact of air pollution on the ocular surface and tear cytokine levels: a multicenter prospective cohort study. *Front Med (Lausanne)*. 2022;9:909330.

41. Niu L, Li L, Xing C, et al. Airborne particulate matter (PM(2.5)) triggers cornea inflammation and pyroptosis via NLRP3 activation. *Ecotoxicol Environ Saf*. 2021;207:111306.

42. Wang Y, Xiong L, Yao Y, et al. The involvement of DRP1-mediated caspase-1 activation in inflammatory response by urban particulate matter in EA.hy926 human vascular endothelial cells. *Environ Pollut*. 2021;287:117369.

43. Thach TQ, Tsang H, Cao P, Ho LM. A novel method to construct an air quality index based on air pollution profiles. *Int J Hyg Environ Health*. 2018;221:17–26.

44. Tang YJ, Chang HH, Chiang CY, et al. A murine model of acute allergic conjunctivitis induced by continuous exposure to particulate matter 2.5. *Invest Ophthalmol Vis Sci*. 2019;60:2118–2126.

45. Lin Z, Liu X, Zhou T, et al. A mouse dry eye model induced by topical administration of benzalkonium chloride. *Mol Vis*. 2011;17:257–264.

46. Nien CJ, Paugh JR, Massei S, Wahlert AJ, Kao WW, Jester JV. Age-related changes in the meibomian gland. *Exp Eye Res*. 2009;89:1021–1027.

47. Xie HT, Sullivan DA, Chen D, Hatton MP, Kam WR, Liu Y. Biomarkers for progenitor and differentiated epithelial cells in the human meibomian gland. *Stem Cells Transl Med*. 2018;7:887–892.

48. Nuwormegbe S, Park NY, Park HJ, Jin Y, Kim SW, Jester JV. Induction of meibocyte differentiation by three-dimensional, Matrigel culture of immortalized human meibomian gland epithelial cells to form acinar organoids. *Ocul Surf*. 2022;26:271–282.

49. Wrobel A, Seltmann H, Fimmel S, et al. Differentiation and apoptosis in human immortalized sebocytes. *J Invest Dermatol*. 2003;120:175–181.

50. Suzuki T, Kitazawa K, Cho Y, et al. Alteration in meibum lipid composition and subjective symptoms due to aging and meibomian gland dysfunction. *Ocul Surf*. 2022;26:310–317.

51. Blanco-Colio LM, Tunon J, Martin-Ventura JL, Egido J. Anti-inflammatory and immunomodulatory effects of statins. *Kidney Int*. 2003;63:12–23.

52. Bunick CG, Milstone LM. The X-ray crystal structure of the keratin 1-keratin 10 helix 2b heterodimer reveals molecular surface properties and biochemical insights into human skin disease. *J Invest Dermatol*. 2017;137:142–150.

53. Ouellet T, Lussier M, Babai F, Lapointe L, Royal A. Differential expression of the epidermal K1 and K10 keratin genes during mouse embryo development. *Biochem Cell Biol*. 1990;68:448–453.

54. Reyes NJ, Yu C, Mathew R, et al. Neutrophils cause obstruction of eyelid sebaceous glands in inflammatory eye disease in mice. *Sci Transl Med*. 2018;10:eaas9164.

55. Mahajan A, Hasikova L, Hampel U, et al. Aggregated neutrophil extracellular traps occlude meibomian glands during ocular surface inflammation. *Ocul Surf*. 2021;20:1–12.

56. Segal AW. How neutrophils kill microbes. *Annu Rev Immunol*. 2005;23:197–223.

57. Miyabe Y, Miyabe C, Mani V, Mempel TR, Luster AD. Atypical complement receptor C5aR2 transports C5a to initiate neutrophil adhesion and inflammation. *Sci Immunol*. 2019;4:eaav5951.

58. Mueller M, Herzog C, Larmann J, et al. The receptor for activated complement factor 5 (C5aR) conveys myocardial ischemic damage by mediating neutrophil transmigration. *Immunobiology*. 2013;218:1131–1138.

59. Li L, Xing C, Zhou J, et al. Airborne particulate matter (PM(2.5)) triggers ocular hypertension and glaucoma through pyroptosis. *Part Fibre Toxicol*. 2021;18:10.

60. Bu J, Zhang M, Wu Y, et al. High-fat diet induces inflammation of meibomian gland. *Invest Ophthalmol Vis Sci*. 2021;62:13.

61. Xu KK, Huang YK, Liu X, Zhang MC, Xie HT. Organotypic culture of mouse meibomian gland: a novel model to study meibomian gland dysfunction in vitro. *Invest Ophthalmol Vis Sci*. 2020;61:30.

62. Parfitt GJ, Lewis PN, Young RD, et al. Renewal of the holocrine meibomian glands by label-retaining, unipotent epithelial progenitors. *Stem Cell Reports*. 2016;7:399–410.

63. Zhang Y, Yin K, Wang D, et al. Polystyrene microplastics-induced cardiotoxicity in chickens via the ROS-driven NF-kappaB-NLRP3-GSDMD and AMPK-PGC-1alpha axes. *Sci Total Environ*. 2022;840:156727.

64. Dong R, Xue Z, Fan G, et al. Pin1 Promotes NLRP3 inflammasome activation by phosphorylation of p38 MAPK pathway in septic shock. *Front Immunol*. 2021;12:620238.

65. Yang DL, Zhang ZN, Liu H, et al. Indoor air pollution and human ocular diseases: associated contaminants and underlying pathological mechanisms. *Chemosphere*. 2022;311:137037.

66. Tomlinson A, Bron AJ, Korb DR, et al. The international workshop on meibomian gland dysfunction: report of the diagnosis subcommittee. *Invest Ophthalmol Vis Sci*. 2011;52:2006–2049.

67. Teo CHY, Ong HS, Liu YC, Tong L. Meibomian gland dysfunction is the primary determinant of dry eye symptoms: analysis of 2346 patients. *Ocul Surf*. 2020;18:604–612.

68. Sun M, Moreno IY, Dang M, VJ Coulson-Thomas. Meibomian gland dysfunction: what have animal models taught us? *Int J Mol Sci*. 2020;21:8822.

69. Kim Y, Choi YH, Kim MK, Paik HJ, Kim DH. Different adverse effects of air pollutants on dry eye disease: ozone, PM(2.5), and PM(10). *Environ Pollut*. 2020;265:115039.

70. Zhou S, Xi Y, Chen Y, et al. Ovarian dysfunction induced by chronic whole-body PM2.5 exposure. *Small*. 2020;16:e2000845.

71. Gaskins AJ, Minguez-Alarcon L, Fong KC, et al. Exposure to fine particulate matter and ovarian reserve among women from a fertility clinic. *Epidemiology*. 2019;30:486–491.

72. Vesterdal LK, Danielsen PH, Folkmann JK, et al. Accumulation of lipids and oxidatively damaged DNA in hepatocytes exposed to particles. *Toxicol Appl Pharmacol*. 2014;274:350–360.

73. Du Z, Hu J, Lin L, et al. Melatonin alleviates PM(2.5)-induced glucose metabolism disorder and lipidome alteration by regulating endoplasmic reticulum stress. *J Pineal Res*. 2022;73:e12823.

74. Yan L, Chen S, Hou C, et al. Multi-omics analysis unravels dysregulated lysosomal function and lipid metabolism involved in sub-chronic particulate matter-induced pulmonary injury. *Sci Total Environ*. 2022;836:155642.

75. Moller P, Mikkelsen L, Vesterdal LK, et al. Hazard identification of particulate matter on vasomotor dysfunction and progression of atherosclerosis. *Crit Rev Toxicol*. 2011;41:339–368.

76. Tien CP, Chen CH, Lin WY, et al. Ambient particulate matter attenuates Sirtuin1 and augments SREBP1-PIR axis to induce human pulmonary fibroblast inflammation: molecular mechanism of microenvironment associated with COPD. *Aging (Albany NY)*. 2019;11:4654–4671.

77. Kim JS, Chen Z, Alderete TL, et al. Associations of air pollution, obesity and cardiometabolic health in young adults: the Meta-AIR study. *Environ Int*. 2019;133:105180.

78. Downie LE, Bandlitz S, Bergmanson JPG, et al. CLEAR - anatomy and physiology of the anterior eye. *Cont Lens Anterior Eye*. 2021;44:132–156.

79. Driver PJ, Lemp MA. Meibomian gland dysfunction. *Surv Ophthalmol*. 1996;40:343–367.

80. Butovich IA, Wilkerson A, Yuksel S. Depletion of cholesteryl esters causes meibomian gland dysfunction-like symptoms in a Soat1-null mouse model. *Int J Mol Sci*. 2021;22:1593.

81. Du YL, Peng X, Liu Y, et al. Ductal hyperkeratinization and acinar renewal abnormality: new concepts on pathogenesis of meibomian gland dysfunction. *Curr Issues Mol Biol*. 2023;45:1889–1901.

82. Borm P, Cassee FR, Oberdorster G. Lung particle overload: old school -new insights? *Part Fibre Toxicol*. 2015;12:10.

83. Yu P, Zhang X, Liu N, Tang L, Peng C, Chen X. Pyroptosis: mechanisms and diseases. *Signal Transduct Target Ther*. 2021;6:128.

84. Du X, Jiang S, Zeng X, et al. Fine particulate matter-induced cardiovascular injury is associated with NLRP3 inflammasome activation in Apo E(-/-) mice. *Ecotoxicol Environ Saf*. 2019;174:92–99.

85. Li M, Hua Q, Shao Y, et al. Circular RNA circBbs9 promotes PM(2.5)-induced lung inflammation in mice via NLRP3 inflammasome activation. *Environ Int*. 2020;143:105976.

86. Hirota JA, Hirota SA, Warner SM, et al. The airway epithelium nucleotide-binding domain and leucine-rich repeat protein 3 inflammasome is activated by urban particulate matter. *J Allergy Clin Immunol*. 2012;129:1116–1125.e1116.

87. Liu C, She Y, Huang J, et al. HMGB1-NLRP3-P2 × 7R pathway participates in PM(2.5)-induced hippocampal neuron impairment by regulating microglia activation. *Ecotoxicol Environ Saf*. 2022;239:113664.

88. Fann DY, Lim YA, Cheng YL, et al. Evidence that NF-kappaB and MAPK signaling promotes NLRP inflammasome activation in neurons following ischemic stroke. *Mol Neurobiol*. 2018;55:1082–1096.

89. Lee DC, Choi H, Oh JM, et al. Urban particulate matter regulates tight junction proteins by inducing oxidative stress via the Akt signal pathway in human nasal epithelial cells. *Toxicol Lett*. 2020;333:33–41.

90. Xin L, Che B, Zhai B, et al. 1,25-Dihydroxy vitamin D(3) attenuates the oxidative stress-mediated inflammation induced by PM(2.5)via the p38/NF-kappaB/NLRP3 pathway. *Inflammation*. 2019;42:702–713.

91. Wang M, Liu Z, Hu S, et al. Taohong Siwu decoction ameliorates ischemic stroke injury via suppressing pyroptosis. *Front Pharmacol*. 2020;11:590453.